

Geophysical Research Letters



RESEARCH LETTER

10.1029/2023GL103696

Key Points:

- We studied elastic properties, plastic deformation, and permeability of northern Hikurangi margin rocks
- We provide a permeability-porosity relationship for accretionary prism mudrocks
- Permeability healing in the Hikurangi accretionary prism rocks provides a mechanism justifying slow-slip event cyclicity

Supporting Information:

Supporting Information may be found in the online version of this article.

Correspondence to:

N. Tisato, nicola.tisato@jsg.utexas.edu

Citation:

Tisato, N., Bland, C. D., Van Avendonk, H., Bangs, N., Garza, H., Alamoudi, O., et al. (2024). Permeability and elastic properties of rocks from the northern Hikurangi margin: Implications for slow-slip events. *Geophysical Research Letters*, *51*, e2023GL103696. https://doi.org/10.1029/2023GL103696

Received 22 AUG 2023 Accepted 22 DEC 2023

Author Contributions:

Conceptualization: Nicola Tisato, Carolyn D. Bland, Harm Van Avendonk, Nathan Bangs, Hector Garza, Omar Alamoudi, Kelly Olsen, Andrew Gase Data curation: Nicola Tisato, Carolyn D. Bland

Formal analysis: Nicola Tisato, Harm Van Avendonk, Hector Garza Funding acquisition: Nicola Tisato, Harm Van Avendonk, Nathan Bangs Investigation: Nicola Tisato, Carolyn D. Bland, Harm Van Avendonk, Nathan Bangs, Kelly Olsen, Andrew Gase Methodology: Nicola Tisato, Carolyn D. Bland, Hector Garza, Omar Alamoudi

© 2024. The Authors.

This is an open access article under the terms of the Creative Commons Attribution License, which permits use, distribution and reproduction in any medium, provided the original work is properly cited.

Permeability and Elastic Properties of Rocks From the Northern Hikurangi Margin: Implications for Slow-Slip Events

Nicola Tisato¹, Carolyn D. Bland^{1,2}, Harm Van Avendonk³, Nathan Bangs³, Hector Garza¹, Omar Alamoudi¹, Kelly Olsen^{3,4}, and Andrew Gase^{3,5}

¹Department of Earth and Planetary Sciences, Jackson School of Geosciences, The University of Texas at Austin, Austin, TX, USA, ²Now at Pariveda Solutions, Dallas, TX, USA, ³Jackson School of Geosciences, Institute for Geophysics, The University of Texas at Austin, Austin, TX, USA, ⁴Now at Descartes Labs, Sante Fe, NM, USA, ⁵Now at Geology Department, Western Washington University, Bellingham, WA, USA

Abstract Fluid flow and pore-pressure cycling are believed to control slow slip events (SSEs), such as those that frequently occur at the northern Hikurangi margin of New Zealand. To better understand fluid flow in the forearc system we examined the relationship between several physical properties of Cretaceous-to-Pliocene sedimentary rocks from the Raukumara peninsula. We found that the permeability of the deep wedge is too low to drain fluids, but fracturing increases permeability by orders of magnitude, making fracturing key for fluid flow. In weeks to months, plastic deformation, swelling, and possibly not-yet-identified mechanisms heal the fractures, restoring the initial permeability. We conclude that overpressures at the northern HM might partly dissipate during SSEs due to enhanced permeability near faults. However, in the months following an SSE, healing in the prism will lower permeability, forcing pore pressure to rise and a new SSE to occur.

Plain Language Summary Earth's crust comprises many tectonic plates fitting together like jigsaw puzzle pieces. Tectonic plates subduct in the mantle along active converging margins, where the forces driving such a convergence can trigger large earthquakes. However, these subduction zones often deform without producing earthquakes, but through slow deformations called slow slip events (SSE). The Hikurangi Margin (HM) of New Zealand is a well-studied subduction zone, producing both earthquakes and SSEs. The northern HM exhibits more frequent and shallower SSEs than the southern margin. Understanding what controls such differences can help improve the general understanding of subduction zone mechanics and earthquakes. One of the hypotheses is that the differences between the deformation of the northern and southern HM are controlled by the pressure of fluids at depth. We tested the elastic and fluid-transport properties of four samples from the northern HM and found that the overriding plate, if not fractured, would be impermeable to fluids. We also tested a fractured sample and observed efficient healing that resets the initial permeability. We conclude that fracturing the overriding plate is fundamental to draining the fluids carried at depth by the subducting plate, and SSEs may create new pathways for fluids to escape to the seafloor.

1. Introduction

At the shallow (<15 km depth) portion of the plate interface of subduction zones, scientists have found that convergence between the tectonic plates is often accommodated by modes of slip in between earthquakes and aseismic creep (Saffer & Wallace, 2015). Slow-slip events (SSEs) represent one class of such transient phenomena, which can lead to several centimeters of slip over several days to months (Schwartz & Rokosky, 2007). The relatively large seismic moment released by shallow SSEs, comparable to that of earthquakes (Passarelli et al., 2021), proves the importance to understand SSEs and how they influence the seismogenic character of a convergent margin. Frictional properties and stress heterogeneities along the plate interface might favor SSEs (Barnes et al., 2020; Bell et al., 2010; Boulton et al., 2019; Im et al., 2020; Leah et al., 2022; Rabinowitz et al., 2018; Shreedharan et al., 2023). Moreover, subducting oceanic crust and sediments release large volumes of fluids whose pressure can exceed hydrostatic conditions when confined within low permeability rocks, lowering the effective stress on the shallow megathrust or splay faults and creating conditions conducive to SSEs (Ellis et al., 2015; Kitajima & Saffer, 2012; Tsuji et al., 2008; Warren-Smith et al., 2019).

TISATO ET AL. 1 of 11

Avendonk, Nathan Bangs Software: Nicola Tisato, Carolyn D. Bland, Omar Alamoudi Supervision: Nicola Tisato, Harm Van Avendonk, Nathan Bangs Validation: Nicola Tisato, Carolyn D. Bland, Harm Van Avendonk, Nathan Bangs, Hector Garza, Omar Alamoudi, Kelly Olsen, Andrew Gase Visualization: Nicola Tisato, Carolyn Writing - original draft: Nicola Tisato, Carolyn D. Bland, Harm Van Avendonk, Nathan Bangs, Hector Garza, Omar Alamoudi, Kelly Olsen, Andrew Gase Writing - review & editing: Nicola Tisato, Carolyn D. Bland, Harm Van Avendonk, Nathan Bangs, Hector Garza, Omar Alamoudi, Kelly Olsen, Andrew

Resources: Nicola Tisato, Harm Van

The northern Hikurangi margin (HM) in New Zealand, is a subduction zone with a shallow forearc and plate interface, where sediment accretion, compaction, and deformation have been modulated for millions of years by underthrusting seamounts (Gase et al., 2021; Sun et al., 2020). Subducting seamounts may cause stress heterogeneities (Bangs et al., 2023; Leah et al., 2022; Sun et al., 2020) and fluid pressure transients (Shaddox & Schwartz, 2019) that can lead to SSEs, several of which have been characterized in great detail by onshore geodetic and offshore absolute pressure gauge (APG) data (Yohler et al., 2019). Offshore Gisborne SSEs occur every 1–2 years and can last several weeks, during which time 5–30 cm of slip may be accommodated (L. Wallace, 2020). Temporal variations in the character of earthquake focal mechanisms within the subducting oceanic crust provide compelling evidence for low effective stress before an SSE (Warren-Smith et al., 2019). This observation suggests that fluid pressure increases enable SSEs and that the slip is accompanied by fluid release. Nevertheless, fluid transport through the accretionary wedge in this deformation cycle is not yet well understood (Antriasian et al., 2018).

The physical properties of accreted sediments of the northern HM and their relationship to slip phenomena have been studied recently using cores and data from IODP expeditions (e.g., Wallace et al., 2019). The resulting studies have shed new light on the frictional properties, shallow dewatering, and faulting near the seafloor (Aretusini et al., 2021; Boulton et al., 2019, 2022; Dutilleul et al., 2021; Fagereng et al., 2019; French & Morgan, 2020; Shreedharan et al., 2022). However, to understand how fluid flow and deformation interplay in the deeper prism, we also must consider the physical properties of older, compacted, and diagenetically mature strata (Bassett et al., 2022; Bland et al., 2015). Here, we present and discuss laboratory testing performed on rock samples from the subaerial northern HM as proxies of deep rocks in the prism to understand fluid transport within the accretionary prism better.

2. Materials and Method

To test the mechanical and transport properties of rocks from the northern HM, we collected and performed experiments on outcrop samples from the Raukumara peninsula (Figure 1; Figure S1 in Supporting Information S1) presenting different ages and degrees of diagenesis. In the central part of the peninsula, we collected a very-fine to fine-grained sandstone from the Jurassic-to-Early Cretaceous Torlesse Supergroup forming the backstop for the accretionary wedge (sample M002) (Adams & Graham, 1996; Mortimer et al., 2014). Just east of sample M002 location, we sampled a calcareous siltstone to very-fine-grained sandstone from the Late Cretaceous-to-Paleocene Tinui Group (sample MT07) that likely represents an early passive margin deposit, now buried in the accretionary wedge (Mortimer et al., 2014). Closer to the East coast, we collected a siltstone (sample GB13) from the middle Miocene Tolaga Group, which sedimented in slope basins after subduction initiated along the HM (van de Lagemaat et al., 2022), and a glauconitic siltstone (sample FB12) from the Pliocene Mangaheia Group.

We determined mineral abundances and assemblages of each sample through X-ray diffraction (XRD) analyses and transmitted light microscopy by preparing 30 μ m-in-thickness thin sections. We prepared cylindrical core plugs with parallel end faces for each sample to estimate density, porosity, compressional and shear ultrasonic wave velocities (i.e., Vp and Vs), and helium gas permeability. Samples were tested for confining pressures (P_c) up to 200 MPa (\sim 12.5 km depth for hydrostatic pore pressure and overburden density of 2.6 g/cm³) and deviatoric vertical force (F_v) \sim 2.6 kN. Each core plug was mounted inside a PVC jacket and between two core holders equipped with ultrasonic transducers and fluid ports to saturate and measure the core permeability. This sample assembly is mounted inside the triaxial cell between the load cell and the vertical force piston. We define the mean stress as $\frac{1}{2} \frac{1}{2} \frac{1}{2}$

We measured ultrasonic velocities using the transmission method at room temperature and a frequency of \sim 800 kHz (Birch, 1960). To understand the effect of saturation on Vp and Vs, we measured the ultrasonic velocities of sample GB13 saturated with water previously chemically equilibrated with the sample. During 30 hr, we recorded the injection of 4.7 ml of this fluid, equivalent to 136% of GB13 pore-space volume.

Sample permeabilities were calculated through the transient method, measuring the pressure equilibration of the helium gas contained in two volumes connected to the sample end-faces and flowing through the sample

TISATO ET AL. 2 of 11

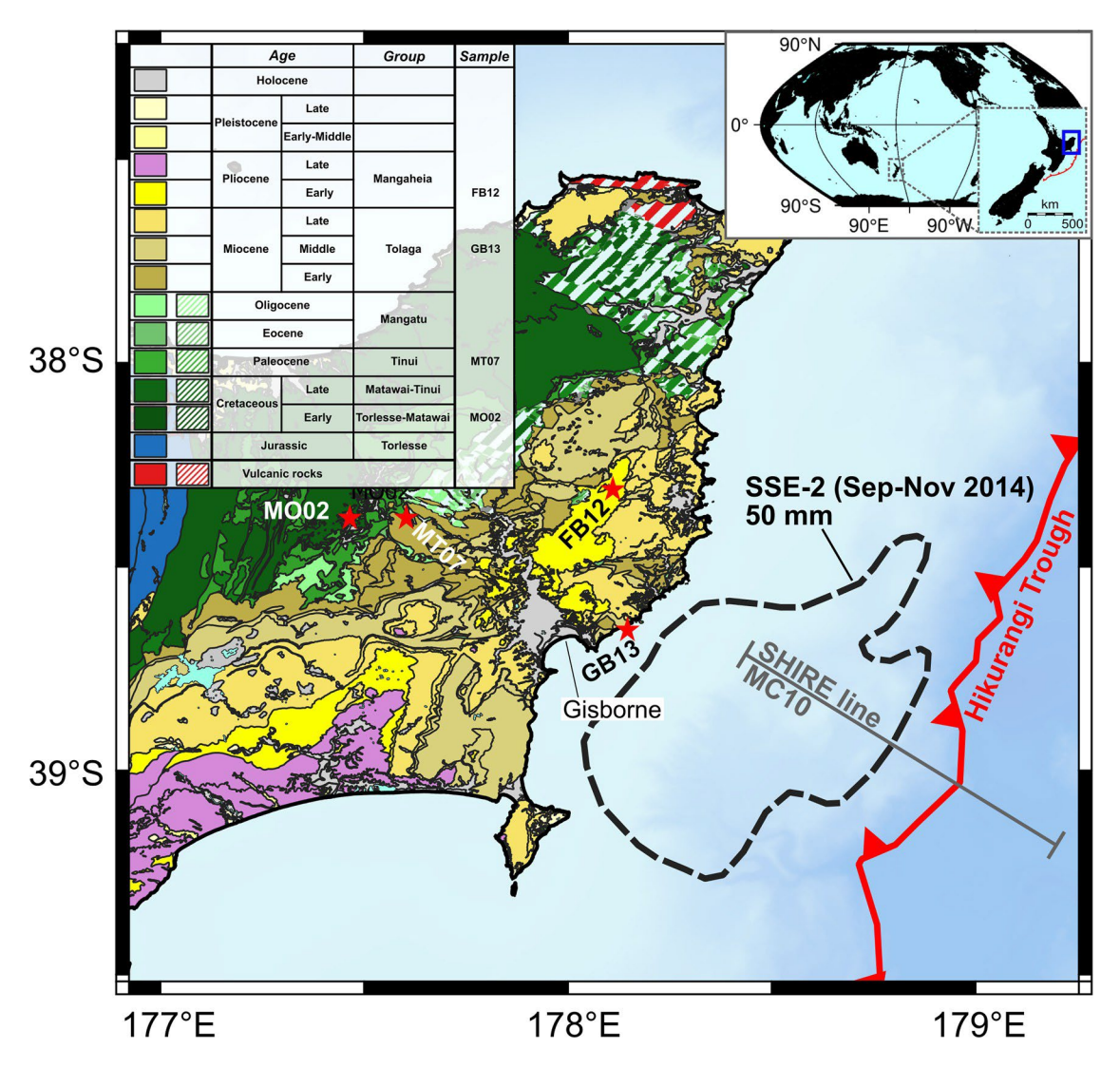


Figure 1. Geologic map of the Raukumara peninsula with the position of our rock samples (Mazengarb & Speden, 2000). The offshore dashed line contour marks the 50 mm geodetic slip model for the September-November 2014 SSE (Warren-Smith et al., 2019). The offshore line indicates the SHIRE project seismic line MC10 (Gase et al., 2021).

(Sutherland & Cave, 1980). To understand the effect of porosity reduction on the permeability of young, loosely consolidated rocks, we assumed FB12 isotropic and measured its permeability during mechanical compaction. First, we measured ultrasonic velocities and permeabilities at P_c up to 70 MPa and σ_d = 5 MPa, then, we increased P_c stepwise to 100, 150, and 200 MPa and waited for 19, 24, and 5 hr to measure creep until the observed shortening rate was less than 1 μ m/hr. Finally, we measured permeability for P_c up to 200 MPa.

To study how fractures influence the permeability of HM rocks, we split sample MT07 through a Brazilian test producing a sub-vertical fracture connecting the opposite end-faces of the core plug. Then, to study the effect of stress on permeability healing, we kept the sample dry and measured permeability as a function of σ' , and we collected three micro-computed tomographies (μ CT) to seek evidence of variations in fracture aperture. A detailed chronology of the operations follows: On day 1, after the Brazilian test, we collected μ CT data set S1. Between day 2 and 9 we performed the first permeability test (kT1) for σ' between 24 and 65 MPa. During kT1 (days 3–5) we promoted healing by keeping σ' to 65 MPa. After kT1 and for the next 39 days, the sample remained inside the pressure vessel at $\sigma'\sim 0$ MPa. Between day 48 and day 77, we performed the second permeability test (kT2) at σ' ranging 5.6–64 MPa. At the end of kT2 we removed the sample from the pressure vessel and acquired μ CT data set S2. Then, the jacketed sample was placed inside a humidity-controlled chamber equipped with a water container and a thermo-hygrometer. For 72 hr, a medium to low vacuum (<0.5 bar) was maintained to promote

TISATO ET AL. 3 of 11

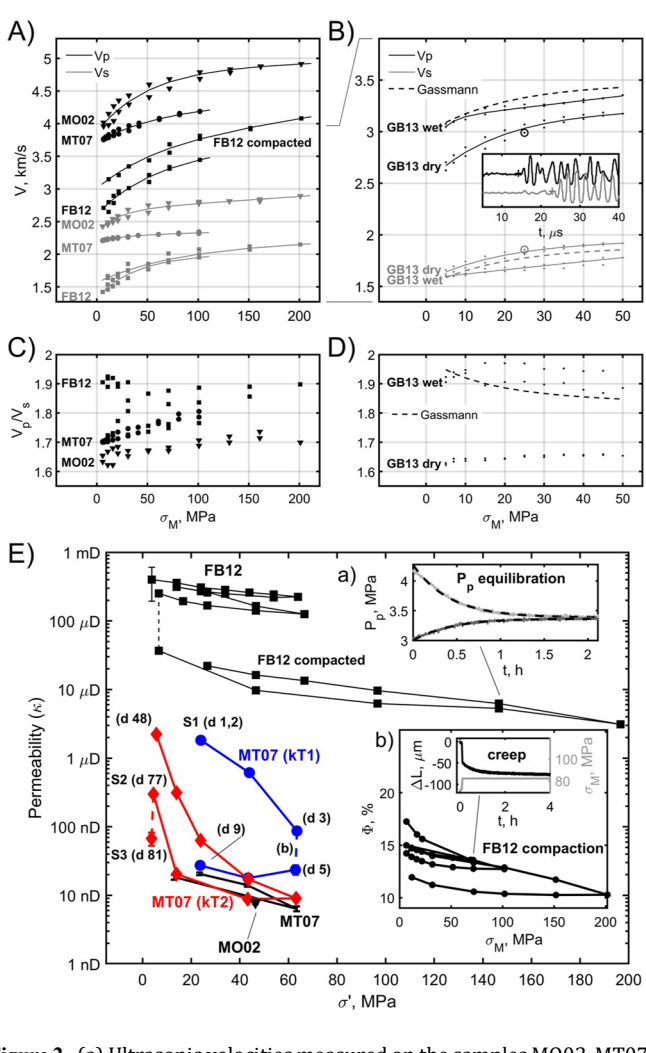


Figure 2. (a) Ultrasonic velocities measured on the samples MO02, MT07 and FB12 as a function of σ_M (b) Ultrasonic velocities for dry and water saturated GB13 sample. Dashed lines indicate the theoretical saturated velocities from Gassmann fluid substitution (Gassmann, 1951). Inset: examples of P and S waveforms recorded at the conditions indicated by the circled dots. (c, d) Vp to Vs ratios for the laboratory data and the fitting curves reported in (a, b), respectively. (e) Permeabilities for samples FB12, MT07, and M002 as a function of σ' . The blue and red curves show the permeability of sample MT07 after fracturing and during two measurement cycles (kT1 and kT2): (d X) near data points indicates X days since stage S1, when the sample was CT-scanned (Figure 3a). After kT1 and kT2, on day 77 is stage S2 when the sample was CT-scanned again and exposed to a humid atmosphere for 72 hr(Figure 3B). Day 81 was stage S3 and the sample was CT-scanned and re-tested for permeability (Figures 3c-3e). (a) Example of pore pressure (Pp) equilibration and fitting curves (dashed lines) for the indicated permeability datapoint. (b) Sample FB12 loss of porosity due to the increase of σ_M . Inset: example of partial compaction due to creep after a σ_M increase.

water evaporation, causing the chamber relative humidity to remain above 97% and activating minerals (e.g., clays and carbonates) with pronounced swelling or dissolution/precipitation properties (Villar et al., 2005). Finally, we acquired μ CT data set S3, and produced a thin section perpendicular to the sample axis, on which we examined the morphology of the fracture for evidence of clay infilling, possibly caused by plastic deformation and triggered by clay swelling.

Each μ CT data set comprises 1600, 33.3 μ m resolution, 16-bits TIFF images perpendicular to the sample axis, recording the entire sample except 4.37 mm at the top and bottom. After normalization and segmentation, we calculated fracture apertures (B) for each CT data set by producing fracture aperture distribution projections (FADP) whose mean and standard deviation provided average apertures (B_m) and associated uncertainties. We report more details on the methods in the Supporting Information S1.

3. Results

The four samples contain more than 35 wt% quartz and feldspars. The remaining minerals are calcite, and clays, of which mica, illites and smectites group minerals (swelling clays) represent at least 13 wt%, while kaolinite and chlorite is up to 5 wt% (Figures S1–S3 in Supporting Information S1). Porosities vary between 7% and 18%, where the tighter samples (MT07 and M002) have a longer diagenetic or metamorphic history. Photomicrographs reveal that the grain size varies significantly among the four samples, except for M002, the large majority of the grains have size <63 μ m, suggesting that our samples are siltstones (i.e., mudrocks) to fine grain sandstones in agreement with the regional geology (Mazengarb & Speden, 2000).

Ultrasonic velocity measurements (Figure 2a) show that Vp and Vs increase with σ_{m} , and the younger samples (FB12 and GB13) generally have lower velocities. Vp to Vs ratios vary between 1.65 and 1.9, with the least consolidated and youngest sample (FB12) exhibiting the highest values. After saturation, sample GB13 Vp increased by ~250 m/s on average while Vs decreased by ~100 m/s on average, increasing the Vp to Vs ratio from ~1.65 to ~1.9.

Before compaction, sample FB12 permeability ranged between 200 and 400 μ D. Then, we raised P_c twice to 70 MPa, causing the permeability to decrease by a factor of two and porosity by 3% (i.e., at $\sigma_m \sim$ 7 MPa, porosity varied from 17.3% to 14.2%). In the following two cycles, where P_c reached 200 MPa, porosity decreased to 13.9%, and the permeability declined by almost an order of magnitude. Concurrently, the ultrasonic Vp increased from 2.6 to 4 km/s.

Samples M002 and MT07, when intact, have permeabilities below 100 nD, regardless of σ' . The permeability of the fractured MT07 evolved between stages S1, S2, and S3. After S1 and during the permeability cycle kT1, the permeability dropped from 2 to 0.087 μ D. After exposing the sample to $\sigma' \sim 65$ MPa for more than 48 hr (Figure 4b), we continued kT1 and found

that the permeability further decreased to 24 nD. The permeability remained \sim 2 orders of magnitude lower than the initial permeability, that is, around 30 nD, when σ' was reduced. After 39 days, the new increase of σ' during the second permeability cycle kT2, caused the permeability to drop to 9 nD. During the following decrease of σ' , the permeability resembled pre-fracturing values. The last measurement of kT2 was performed at σ' = 4.5 MPa and permeability was 300 nD, seven times lower than the initial value measured at σ' = 5.6 MPa. After exposing the sample to humidity for 72 hr, the permeability, measured at σ' = 3.7 MPa, decreased to 67 nD.

TISATO ET AL. 4 of 11

19448007, 2024, 2, Downloaded from https://agupubs.onlinelibrary.wiley.com/doi/10.1029/2023GL103696 by University Of Texas at Austin, Wiley Online Library on [08/04/2024]. See the Terms and Conditions (https://onlinelibrary.wiley.com/terms

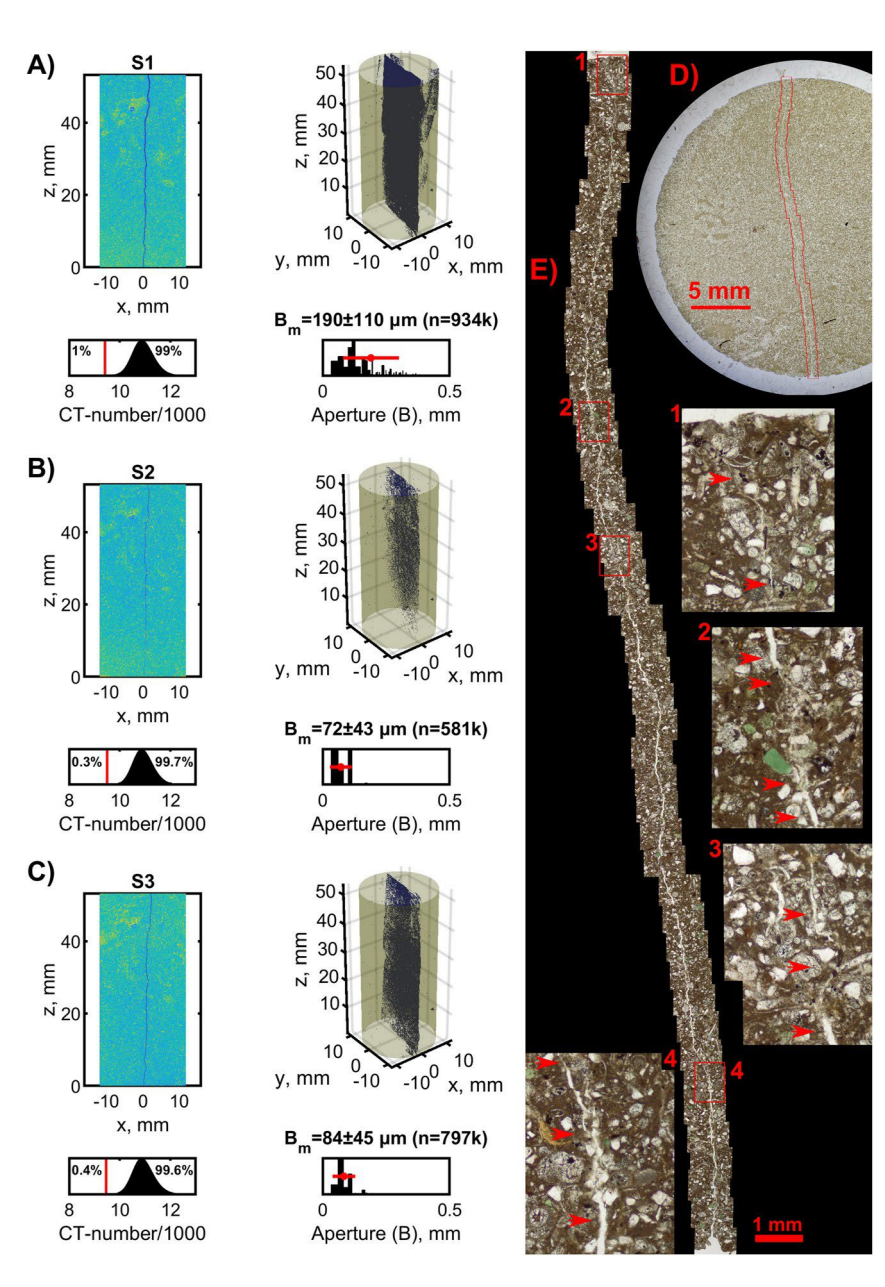


Figure 3. CT-scan and photomicrographs of sample MT07 after fracturing. (a–c) are CT-scans at stages S1, S2, and S3, respectively. Top-left insets report the vertical section of the CT-scan model after normalization (Figure S4 in Supporting Information S1). CT-number distribution is shown in the bottom-left inset. The red vertical line indicates t_x (Equation S5 in Supporting Information S1) and the percentages indicate the relative quantity of voxels representing air (on the left) and solid rock (on the right), respectively. The right top inset in each panel shows the binarized 3D model, where voxels within the fracture are blue. The bottom right insets show the aperture distribution (b), the calculated average and standard deviation (B_m and horizontal red bar), and the total count of voxel within the fracture (n). Panel (d) is a photomicrograph of the thin section at stage S3. Panel E reports zooms from panel (d) Insets 1 to 4 show fracture infill, which are highlighted by red arrows along with open fractures. Panel (e) original image is included in the data repository (resolution = 0.31 μm/pixel).

Visual inspection and analyses on CT-scans reveal that B_m varied from 190 ± 110 µm, to 72 ± 43 µm and 84 ± 45 µm during stages S1, S2, and S3, respectively (Figures 3a–3c). During the same stages, the number of voxels counted within the fracture varied from ~934,000 to ~581,000 and ~797,000. Photomicrographs of sample MT07 at stage S3 show that in several loci, the fracture collapsed, and a fine-grained amorphous mass infilled the fracture (Figures 3d and 3e). These observations suggest that varying confining pressure and humidification caused plastic deformation of clay minerals and swelling, partially closing the fracture and reducing the permeability.

TISATO ET AL. 5 of 11

19448007, 2024, 2, Downloaded from https://agupubs.onlinelibrary.wiley.com/doi/10.1029/2023GL103696 by University Of Texas at Austin, Wiley Online Library on [08/04/2024]. See the Terms

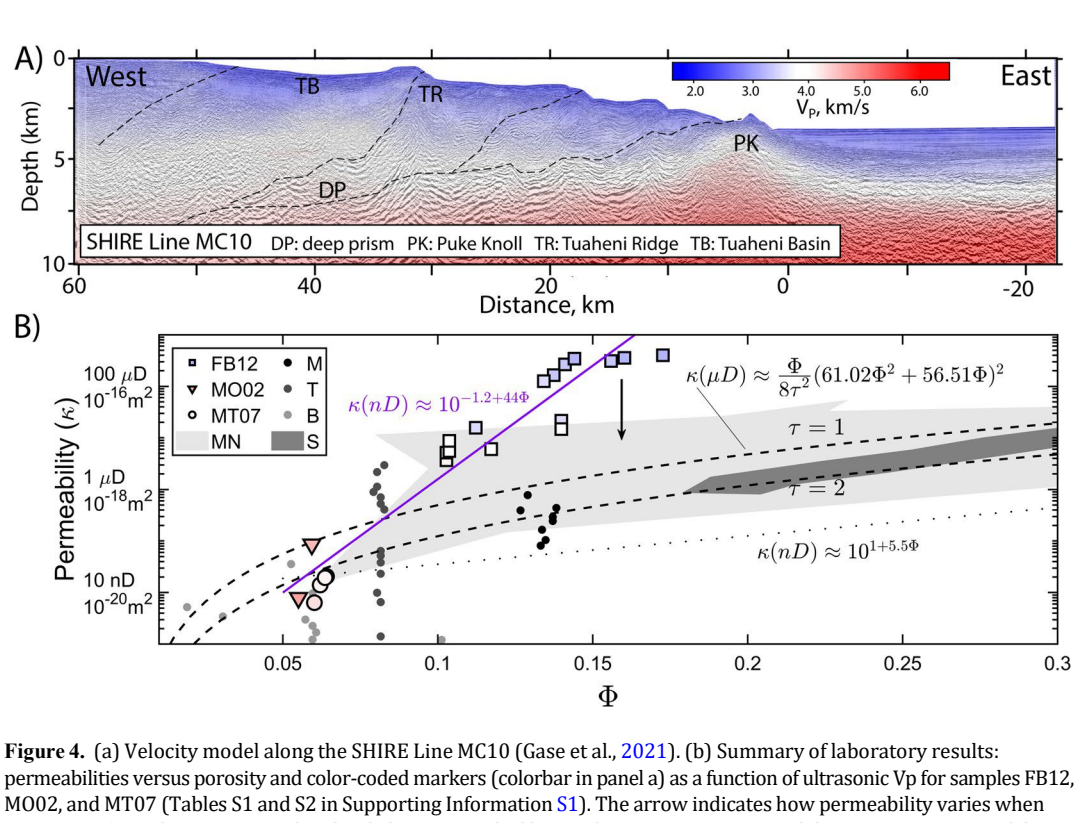


Figure 4. (a) Velocity model along the SHIRE Line MC10 (Gase et al., 2021). (b) Summary of laboratory results: permeabilities versus porosity and color-coded markers (colorbar in panel a) as a function of ultrasonic Vp for samples FB12, MO02, and MT07 (Tables S1 and S2 in Supporting Information S1). The arrow indicates how permeability varies when tests are performed using water rather than helium gas. Dashed lines indicate Equation 3 permeability versus porosity model. The dotted line represents an average permeability for unconsolidated clays and possibly a lower bound for the permeability of HM sediments (Equation 1, Neuzil, 1994). S data (dark-gray area) are for siltstones (Reece et al., 2012). The continuous line (Equation 2) fits our data and agrees with measured mudrock permeabilities indicated by the MN gray-shaded area (Magara, 1978; Neglia, 1979). Such a line also represents an upper bound for the permeability of HM rocks. M, T, and B data are permeabilities measured in boreholes (M: Reisdorf et al. (2016), Yu et al. (2017); T: Boisson et al. (2001); B: Intera Eng. Ltd. (2011), Roberts et al. (2011), Walsh (2011)).

4. Discussion

We provide porosity-permeability relationships for rock samples from the subaerial northern HM under various confining pressures. Ultrasonic velocities of dry samples are similar to the seismic velocities estimated offshore New Zealand by the SHIRE project (Gase et al., 2021). The seismic reflectivity imaged along the transect MC10 shows the décollement and several splay faults that may partly accommodate the convergence (Figure 4a). Inside the prism, Vp increases from 2.0 km/s near the surface to 4.5 km/s at the prism base ~7 km below sea level. The comparison between the seismic and ultrasonic velocities (Figure 4b) suggests that sample FB12 and possibly sample GB13 represent the modern slope basins on the outer prism, consistent with their depositional environment. Deeper in the prism, Vp reaches 4.5 km/s as compaction and diagenesis must have hardened the rock (Dvorkin & Nur, 1996; Saxena & Mavko, 2014). The ultrasonic velocities of the Tinui group sample (MT07) correspond well to the velocities of the deep part of the prism, which is in agreement with the idea that these Paleocene rocks form the base of the prism (Mazengarb & Speden, 2000; Nicol et al., 2007). At 150 MPa (~7 km depth), the ultrasonic Vp of the Torlesse sample (MO02) is 4.8 km/s, which is higher than what we imaged in the deep prism on Line MC10 (Figure 4), suggesting that there may not be a deep offshore portion of the Torlesse basement offshore northern HM (Bassett et al., 2022; Gase et al., 2021).

The seismic to ultrasonic velocities comparison (Figure 4) is semi-quantitative as uncertainty is introduced by frequency differences and microcracks produced during sample preparation (Eberhart-Phillips et al., 1989; Tsuji & Iturrino, 2008). Velocities in section MC10 and our samples have been measured at frequencies around 20 and 800,000 Hz, respectively. Considering the frequency range, a typical P-wave quality factor between 30 and 150, and a nearly-constant Q model (Liu et al., 1976; Tisato et al., 2021), we should expect velocity dispersion between 2.3% and 12%. Conversely, SHIRE and laboratory data were collected on saturated and dry samples, respectively. Saturation increases P-wave velocities of sample GB13 by ~10%, suggesting that the effect of fluid saturation and

TISATO ET AL. 6 of 11

anelasticity on velocities should counteract each other. Given the similarity in P-wave velocities and depositional environment, we suggest that the Tinui and Tolaga group rocks (MT07 and GB13) are good lithological proxies for the deep and shallow offshore Hikurangi prism, respectively.

Our sample permeabilities range from 1 nD to 1 mD, with the samples representing the deep part of the prism being the tightest. Neuzil (1994, 2019) compiled data from several studies on unconsolidated clays with a maximum porosity of 80%, and consolidated mudrocks with porosities <35%. Saffer and Bekins (1998) followed Neuzil's work and described the permeability (κ) of the Nankai accretionary complex as:

$$22(2222) \approx 10^{1+5.500} \tag{1}$$

which fits the porosity-permeability relationship of unconsolidated sediments and is a lower bound for the permeability of mudrocks similar to our samples (Magara, 1978; Neglia, 1979; Reece et al., 2012). On the other hand, we found that:

$$2P(PPP) \approx 10^{-1.2+4400}$$
 (2)

fits our results and is an upper bound for the permeability of mudrocks. We suggest that Equation 2 (Figure 4b) overestimate permeabilities in the Northern Hikurangi accretionary prism at depths >1 km because helium gas is not as efficient as seawater in activating swelling clays, whose expansion lowers the effective permeabilities (Villar et al., 2005); At burial depths >1–2 km, the porosity of clay-bearing sediments and mudrocks drops below 35% (Griffiths & Joshi, 1989; Magara, 1978; Skempton, 1969). Permeabilities measured in boreholes are typically orders of magnitude higher than those measured in the laboratory due to the presence of fractures (Figure 4b lines M,T,B) (Neuzil, 2019), and numerical models of permeability in microfractured claystones agree with the mudrocks porosity-permeability in Figure 4b (Vora & Dugan, 2019). Therefore, we propose that the permeability of mudrocks, similar to those the Northern Hikurangi accretionary prism, can be described by a Kozeny-Carman relation (dashed lines in Figure 4b):

$$\Box \Box = \frac{\Box \Box}{8\Box \Box^2} \Box \Box^2 \tag{3}$$

Where τ is tortuosity, and R is the median pore diameter (Carman, 1997). We obtained R(nm) = $61.02\phi^2 + 56.51\phi$ from data reported by Hunt (1996) for mudrocks.

Every 1–2 years, the northern HM experiences an SSE that lasts several weeks (L. Wallace, 2020). Recent analyses of the APG data offshore Gisborne have shown that the 2014 SSE may have experienced up to 30 cm of slip in the center of a \sim 100 km wide patch, though less displacement is expected along the edges (Yohler et al., 2019). Some authors have suggested that SSEs that originate along the decollement at the base of the wedge are accompanied by slip diverted to thrust faults in the Hikurangi accretionary wedge (Shaddox & Schwartz, 2019). We expect SSEs to fracture the rocks, deform and cause granular flow along these thrust faults (Chen, 2023; Fagereng et al., 2019; Morgan et al., 2022). Our pre and post-failure laboratory measurements suggest that these processes might increase the deeper prism permeability, where MT07 equivalent rocks may be present, by 2–3 orders of magnitude.

The fractured sample MT07 regained its pre-fracturing permeability over the course of several weeks. Between stages S1 and S2, the permeability recovery was achieved in dry conditions, possibly through visco-plastic deformation -also observed in sample FB12- and likely concentrated near soft minerals such as clays (Mondol et al., 2008). Between stages S2 and S3 (humidification), the permeability decreased by a factor of 5 while the fracture aperture increased, which could be explained by clay swelling, mineral softening, and dissolution and precipitation of carbonates (Cadoret, 1993; Erguler & Ulusay, 2009; Galibert, 2016; Vanorio et al., 2008). Once confined, softened minerals and hydrated clays deform and clog the fracture more efficiently than dry minerals, explaining the permeability loss. Further investigating the permeability loss in rock samples is beyond the scope of the paper, but we suggest that permeability healing also affects HM faults especially above the 5–7 km deep temperature-controlled smectite-illite transition (Antriasian et al., 2018; Freed & Peacor, 1989; Pecher et al., 2017; Tisato & Marelli, 2013).

In the Hikurangi subduction zone, fluids expelled from pore space and fluids released by dehydration reactions travel along the plate interface or through the accretionary wedge (Ellis et al., 2015). As the fluid pressure

TISATO ET AL. 7 of 11

Wiley Online Library on [08/04/2024]. See the Tern

increases near the decollement and inside the accretionary wedge, conditions may become favorable for an SSE (Burgreen-Chan et al., 2016; Kobayashi & Sato, 2021). Though this mechanism has been proposed for several subduction zones where SSE occur at larger depths (Audet et al., 2009; Kodaira et al., 2004), the analysis of Warren-Smith et al. (2019) on the northern HM, is also compatible with the sealing of fluid pathways after an SSE. The expansion and plastic deformation of clays may provide an efficient mechanism to reduce permeability over weeks or months after an SSE.

Shreedharan et al. (2023) studied sediments collected above the décollement of the Hikurangi margin, showing that their strength recovers little after shear testing. Minimal shear strength recovery is conducive to SSEs because it limits the accumulation of elastic energy from tectonic forces. Post-SSE permeability healing controls the development and recovery of pre-SSE overpressures, which together with a low mechanical strength, will set favorable conditions for a new SSE.

5. Conclusions

We provided relationships between porosity, permeability, and confining pressure for rocks that make up the accretionary prism of the northern HM. We suggest an empirical porosity-permeability relationship (Equation 3) to model fluid transport and estimate effective stress in shallow subduction zones. Mechanical failure of siltstones enhances permeability, but for several weeks, healing reduces the permeability again, suggesting that after an SSE, sediments deep in the northern HM accretionary prism can recover permeability efficiently within the time frame of an SSE as a mechanism explaining the regular recurrence of these events.

Data Availability Statement

Data is available at Tisato (2022).

References

Adams, C. J., & Graham, I. J. (1996). Metamorphic and tectonic geochronology of the Torlesse Terrane, Wellington, New Zealand. New Zealand Journal of Geology and Geophysics, 39(2), 157–180. https://doi.org/10.1080/00288306.1996.9514703

Antriasian, A., Harris, R. N., Tréhu, A. M., Henrys, S. A., Phrampus, B. J., Lauer, R., et al. (2018). Thermal regime of the northern Hikurangi margin, New Zealand. *Geophysical Journal International*. https://doi.org/10.1093/gji/ggy450

Aretusini, S., Meneghini, F., Spagnuolo, E., Harbord, C. W., & Di Toro, G. (2021). Fluid pressurisation and earthquake propagation in the Hikurangi subduction zone. *Nature Communications*, *12*(1), 2481. https://doi.org/10.1038/s41467-021-22805-w

Audet, P., Bostock, M. G., Christensen, N. I., & Peacock, S. M. (2009). Seismic evidence for overpressured subducted oceanic crust and megathrust fault sealing. *Nature*, 457(7225), 76–78. https://doi.org/10.1038/nature07650

Bangs, N. L., Morgan, J. K., Bell, R. E., Han, S., Arai, R., Kodaira, S., et al. (2023). Slow slip along the Hikurangi margin linked to fluid-rich sediments trailing subducting seamounts. *Nature Geoscience*, 16(6), 505–512. https://doi.org/10.1038/s41561-023-01186-3

Barnes, P. M., Wallace, L. M., Saffer, D. M., Bell, R. E., Underwood, M. B., Fagereng, A., et al. (2020). Slow slip source characterized by lithological and geometric heterogeneity. *Science Advances*, 6(13). https://doi.org/10.1126/sciadv.aay3314

Bassett, D., Arnulf, A., Henrys, S., Barker, D., Avendonk, H., Bangs, N., et al. (2022). Crustal structure of the Hikurangi Margin from SHIRE seismic data and the relationship between forearc structure and shallow Megathrust Slip Behavior. *Geophysical Research Letters*, 49(2), e2021GL096960. https://doi.org/10.1029/2021GL096960

Bell, R., Sutherland, R., Barker, D. H. N., Henrys, S., Bannister, S., Wallace, L., & Beavan, J. (2010). Seismic reflection character of the Hikurangi subduction interface, New Zealand, in the region of repeated Gisborne slow slip events. *Geophysical Journal International*, 180(1), 34–48. https://doi.org/10.1111/j.1365-246X.2009.04401.x

Birch, F. (1960). The velocity of compressional waves in rocks to 10 kilobars: 1. *Journal of Geophysical Research*, 65(4), 1083–1102. https://doi.org/10.1029/JZ065i004p01083

Bland, K. J., Uruski, C. I., & Isaac, M. J. (2015). Pegasus Basin, eastern New Zealand: A stratigraphic record of subsidence and subduction, ancient and modern. New Zealand Journal of Geology and Geophysics, 58(4), 319–343. https://doi.org/10.1080/00288306.2015.1076862

Boisson, J.-Y., Bertrand, L., Heitz, J.-F., & Golvan, Y. (2001). In situ and laboratory investigations of fluid flow through an argillaceous formation at different scales of space and time, Tournemire tunnel, southern France. *Hydrogeology Journal*, 9(1), 108–123. https://doi.org/10.1007/s100400000119

Boulton, C., Mizera, M., Niemeijer, A. R., Little, T. A., Müller, I. A., Ziegler, M., & Hamers, M. F. (2022). Observational and theoretical evidence for frictional-viscous flow at shallow crustal levels. *Lithos*, 428–429, 106831. https://doi.org/10.1016/j.lithos.2022.106831

Boulton, C., Niemeijer, A. R., Hollis, C. J., Townend, J., Raven, M. D., Kulhanek, D. K., & Shepherd, C. L. (2019). Temperature-dependent frictional properties of heterogeneous Hikurangi Subduction Zone input sediments, ODP Site 1124. *Tectonophysics*, 757, 123–139. https://doi.org/10.1016/j.tecto.2019.02.006

Burgreen-Chan, B., Meisling, K. E., & Graham, S. (2016). Basin and petroleum system modelling of the East Coast Basin, New Zealand: A test of overpressure scenarios in a convergent margin. *Basin Research*, 28(4), 536–567. https://doi.org/10.1111/bre.12121

Cadoret, T. (1993). Effet de la saturation eau-gaz sur les proprietes acoustiques des roches. (PhD Thesis) (Vol. 7). Université Paris Diderot—Paris. Retrieved from http://www.theses.fr/1993PA077130

Carman, P. C. (1997). Fluid flow through granular beds. Chemical Engineering Research and Design, 75, S32–S48. https://doi.org/10.1016/S0263-8762(97)80003-2

TISATO ET AL. 8 of 11

Acknowledgments

We thank editor Lucy Flesh, and reviewers Carolyn Boulton, Ake Fagereng, and one anonymous, Luc Lavier and Dominic Strogen for discussions. NSF supported this research (OCE-1949171).



Geophysical Research Letters

- 10.1029/2023GL103696
- Chen, J. (2023). The emergence of four types of slow slip cycles on dilatant, fluid saturated faults. *Journal of Geophysical Research: Solid Earth,* 128(2), e2022JB024382. https://doi.org/10.1029/2022JB024382
- Dutilleul, J., Bourlange, S., & Géraud, Y. (2021). Porosity and compaction state at the active Pāpaku thrust fault in the frontal accretionary wedge of the north Hikurangi margin. *Geochemistry, Geophysics, Geosystems*, 22(10), e2020GC009325. https://doi.org/10.1029/2020GC009325 Dvorkin, J., & Nur, A. (1996). Elasticity of high-porosity sandstones: Theory for two North Sea data sets. *Geophysics*, 61(5), 1363–1370. https://doi.org/10.1190/1.1444059
- Eberhart-Phillips, D., Han, D.-H., & Zoback, M. D. (1989). Empirical relationships among seismic velocity, effective pressure, porosity, and clay content in sandstone. *Geophysics*, 54(1), 82–89. https://doi.org/10.1190/1.1442580
- Ellis, S., Fagereng, Å., Barker, D., Henrys, S., Saffer, D., Wallace, L., et al. (2015). Fluid budgets along the northern Hikurangi subduction margin, New Zealand: The effect of a subducting seamount on fluid pressure. *Geophysical Journal International*, 202(1), 277–297. https://doi.org/10.1093/gji/ggy127
- Erguler, Z. A., & Ulusay, R. (2009). Water-induced variations in mechanical properties of clay-bearing rocks. *International Journal of Rock Mechanics and Mining Sciences*, 46(2), 355–370. https://doi.org/10.1016/j.ijrmms.2008.07.002
- Fagereng, Å., Savage, H. M., Morgan, J. K., Wang, M., Meneghini, F., Barnes, P. M., et al. (2019). Mixed deformation styles observed on a shallow subduction thrust, Hikurangi margin, New Zealand. *Geology*, 47(9), 872–876. https://doi.org/10.1130/G46367.1
- Freed, R. L., & Peacor, D. R. (1989). Variability in temperature of the smectite/illite reaction in Gulf Coast sediments. Clay Minerals, 24(2), 171–180. https://doi.org/10.1180/claymin.1989.024.2.05
- French, M. E., & Morgan, J. K. (2020). Pore fluid pressures and strength contrasts maintain frontal fault activity, northern Hikurangi margin, New Zealand. *Geophysical Research Letters*. 47(21), e2020GL089209, https://doi.org/10.1029/2020GL089209
- Galibert, P. (2016). Quantitative estimation of water storage and residence time in the epikarst with time-lapse refraction seismic. *Geophysical Prospecting*, 64(2), 431–444. https://doi.org/10.1111/1365-2478.12272
- Gase, A. C., Van Avendonk, H. J. A., Bangs, N. L., Bassett, D., Henrys, S. A., Barker, D. H. N., et al. (2021). Crustal structure of the northern Hikurangi margin, New Zealand: Variable accretion and overthrusting plate strength influenced by rough subduction. *Journal of Geophysical Research: Solid Earth*, 126(5), e2020JB021176. https://doi.org/10.1029/2020JB021176
- Gassmann, F. (1951). Elastic waves through a packing of spheres. Geophysics, 16(4), 673-685. https://doi.org/10.1190/1.1437718
- Griffiths, F. J., & Joshi, R. C. (1989). Change in pore size distribution due to consolidation of clays. *Géotechnique*, 39(1), 159–167. https://doi.org/10.1680/geot.1989.39.1.159
- Hunt, J. M. (1996). Petroleum geochemistry and geology (2nd ed.). W.H. Freeman.
- Im, K., Saffer, D., Marone, C., & Avouac, J. P. (2020). Slip-rate-dependent friction as a universal mechanism for slow slip events. *Nature Geoscience*, 13(10), 705–710. https://doi.org/10.1038/s41561-020-0627-9
- Intera Eng. Ltd. (2011). Descriptive geosphere site model. Intera Engineering Ltd.
- Kitajima, H., & Saffer, D. M. (2012). Elevated pore pressure and anomalously low stress in regions of low frequency earthquakes along the Nankai Trough subduction megathrust: Low stress at low seismic velocity zone. *Geophysical Research Letters*, 39(23), L23301. https://doi.org/10.1029/2012GL053793
- Kobayashi, T., & Sato, T. (2021). Estimating effective normal stress during slow slip events from slip velocities and shear stress variations. Geophysical Research Letters, 48(20), e2021GL095690. https://doi.org/10.1029/2021GL095690
- Kodaira, S., Iidaka, T., Kato, A., Park, J.-O., Iwasaki, T., & Kaneda, Y. (2004). High pore fluid pressure may cause silent slip in the Nankai Trough. *Science*, 304(5675), 1295–1298. https://doi.org/10.1126/science.1096535
- Leah, H., Fagereng, Å., Bastow, I., Bell, R., Lane, V., Henrys, S., et al. (2022). The northern Hikurangi margin three-dimensional plate interface in New Zealand remains rough 100 km from the trench. *Geology*, 50(11), 1256–1260. https://doi.org/10.1130/G50272.1
- Liu, H.-P., Anderson, D. L., & Kanamori, H. (1976). Velocity dispersion due to anelasticity; implications for seismology and mantle composition. Geophysical Journal International, 47(1), 41–58. https://doi.org/10.1111/j.1365-246X.1976.tb01261.x
- Magara, K. (1978). Compaction and fluid migration: Practical petroleum geology. Elsevier Scientific Pub. Co. Distributors for the U.S. and Can, Elsevier North-Holland.
- Mazengarb, C., & Speden, I. G. (2000). *Geology of the Raukumara area. Geological map 6 60.* Lower Hutt: Institute of Geological & Nuclear Sciences. p. + 1 fold. map.
- Mondol, N. H., Bjørlykke, K., & Jahren, J. (2008). Experimental compaction of clays: Relationship between permeability and petrophysical properties in mudstones. *Petroleum Geoscience*, *14*(4), 319–337. https://doi.org/10.1144/1354-079308-773
- Morgan, J. K., Solomon, E. A., Fagereng, A., Savage, H. M., Wang, M., Meneghini, F., et al. (2022). Seafloor overthrusting causes ductile fault deformation and fault sealing along the northern Hikurangi margin. *Earth and Planetary Science Letters*, 593, 117651. https://doi.org/10.1016/j.epsl.2022.117651
- Mortimer, N., Rattenbury, M., King, P., Bland, K., Barrell, D., Bache, F., et al. (2014). High-level stratigraphic scheme for New Zealand rocks. New Zealand Journal of Geology and Geophysics, 57(4), 402–419. https://doi.org/10.1080/00288306.2014.946062
- Neglia, S. (1979). Migration of fluids in sedimentary Basins1. AAPG Bulletin, 63(4), 573–597. https://doi.org/10.1306/2F918194-16CE-11D7-8645000102C1865D
- Neuzil, C. E. (1994). How permeable are clays and shales? Water Resources Research, 30(2), 145–150. https://doi.org/10.1029/93WR02930
 Neuzil, C. E. (2019). Permeability of clays and shales. Annual Review of Earth and Planetary Sciences, 47(1), 247–273. https://doi.org/10.1146/annurev-earth-053018-060437
- Nicol, A., Mazengarb, C., Chanier, F., Rait, G., Uruski, C., & Wallace, L. (2007). Tectonic evolution of the active Hikurangi subduction margin, New Zealand, since the Oligocene: Hikurangi subduction margin tectonics. *Tectonics*, 26(4), TC4002. https://doi.org/10.1029/2006TC002090 Passarelli, L., Selvadurai, P. A., Rivalta, E., & Jónsson, S. (2021). The source scaling and seismic productivity of slow slip transients. *Science Advances*, 7(32), eabg9718. https://doi.org/10.1126/sciadv.abg9718
- Pecher, I. A., Villinger, H., Kaul, N., Crutchley, G. J., Mountjoy, J. J., Huhn, K., et al. (2017). A fluid pulse on the Hikurangi subduction margin: Evidence from a heat flux transect across the upper limit of gas hydrate stability. *Geophysical Research Letters*, 44(24), 12385–12395. https://doi.org/10.1002/2017GL076368
- Rabinowitz, H. S., Savage, H. M., Skarbek, R. M., Ikari, M. J., Carpenter, B. M., & Collettini, C. (2018). Frictional behavior of input sediments to the Hikurangi trench, New Zealand. *Geochemistry*, *Geophysics*, *Geosystems*, 19(9), 2973–2990. https://doi.org/10.1029/2018GC007633
- Reece, J. S., Flemings, P. B., Dugan, B., Long, H., & Germaine, J. T. (2012). Permeability-porosity relationships of shallow mudstones in the Ursa basin, northern deepwater Gulf of Mexico: Mudstone permeability-porosity behavior. *Journal of Geophysical Research*, 117(B12), B12102. https://doi.org/10.1029/2012JB009438
- Reisdorf, A. G., Hostettler, B., Jaeggi, D., Deplazes, G., Blaesi, H., Morard, A., et al. (2016). Litho- and biostratigraphy of the 250 m-deep Mont Terri BDB-1 borehole through the Opalinus clay and bounding formations. https://doi.org/10.13140/RG.2.2.15045.04322

TISATO ET AL. 9 of 11



- Roberts, R., Chace, D., Beauheim, R., & Avis, J. (2011). *Analysis of straddle-packer tests in DGR boreholes (Technical report No. TR-08-32)*. Geofirma Engineering Ltd.
- Saffer, D. M., & Bekins, B. A. (1998). Episodic fluid flow in the Nankai accretionary complex: Timescale, geochemistry, flow rates, and fluid budget. *Journal of Geophysical Research*, 103(B12), 30351–30370. https://doi.org/10.1029/98JB01983
- Saffer, D. M., & Wallace, L. M. (2015). The frictional, hydrologic, metamorphic and thermal habitat of shallow slow earthquakes. *Nature Geoscience*, 8, 594–600. https://doi.org/10.1038/ngeo2490
- Saxena, N., & Mavko, G. (2014). Exact equations for fluid and solid substitution. *Geophysics*, 79(3), L21-L32. https://doi.org/10.1190/geo2013-0187.1
- Schwartz, S. Y., & Rokosky, J. M. (2007). Slow slip events and seismic tremor at circum-Pacific subduction zones. *Reviews of Geophysics*, 45(3), RG3004. https://doi.org/10.1029/2006RG000208
- Shaddox, H. R., & Schwartz, S. Y. (2019). Subducted seamount diverts shallow slow slip to the forearc of the northern Hikurangi subduction zone, New Zealand. *Geology*, 47(5), 415–418. https://doi.org/10.1130/G45810.1
- Shreedharan, S., Ikari, M., Wood, C., Saffer, D., Wallace, L., & Marone, C. (2022). Frictional and lithological controls on shallow slow slip at the northern Hikurangi margin. *Geochemistry, Geophysics, Geosystems*, 23(2), e2021GC010107. https://doi.org/10.1029/2021GC010107
- Shreedharan, S., Saffer, D., Wallace, L. M., & Williams, C. (2023). Ultralow frictional healing explains recurring slow slip events. *Science*, 379(6633), 712–717. https://doi.org/10.1126/science.adf4930
- Skempton, A. W. (1969). The consolidation of clays by gravitational compaction. Quarterly Journal of the Geological Society, 125(1-4), 373-2411. https://doi.org/10.1144/gsjgs.125.1.0373
- Sun, T., Saffer, D., & Ellis, S. (2020). Mechanical and hydrological effects of seamount subduction on megathrust stress and slip. *Nature Geoscience*, 13(3), 249–255. https://doi.org/10.1038/s41561-020-0542-0
- Sutherland, H. J., & Cave, S. P. (1980). Argon gas permeability of New Mexico rock salt under hydrostatic compression. *International Journal of Rock Mechanics and Mining Sciences & Geomechanics Abstracts*, 17(5), 281–288. https://doi.org/10.1016/0148-9062(80)90810-4
- Tisato, N. (2022). Physical properties of Hikurangi margin rocks (version V8) [Dataset]. Texas Data Repository. https://doi.org/10.18738/T8/RMXMIO
- Tisato, N., Madonna, C., & Saenger, E. H. (2021). Attenuation of seismic waves in partially saturated Berea sandstone as a function of frequency and confining pressure. Frontiers in Earth Science, 9, 641177. https://doi.org/10.3389/feart.2021.641177
- Tisato, N, & Marelli, S. (2013). Laboratory measurements of the longitudinal and transverse wave velocities of compacted bentonite as a function of water content, temperature, and confining pressure: Elastic properties of bentonite. *Journal of Geophysical Research: Solid Earth, 118*(7), 3380–3393. https://doi.org/10.1002/jgrb.50252
- Tsuji, T., & Iturrino, G. J. (2008). Velocity-porosity relationships in oceanic basalt from eastern flank of the Juan de Fuca Ridge: The effect of crack closure on seismic velocity. *Exploration Geophysics*. 39(1), 41–51, https://doi.org/10.1071/EG08001
- Tsuji, T., Tokuyama, H., Costa Pisani, P., & Moore, G. (2008). Effective stress and pore pressure in the Nankai accretionary prism off the Muroto Peninsula, southwestern Japan. *Journal of Geophysical Research*, 113(B11), B11401. https://doi.org/10.1029/2007JB005002
- van de Lagemaat, S. H. A., Mering, J. A., & Kamp, P. J. J. (2022). Geochemistry of syntectonic carbonate veins within Late Cretaceous turbidites, Hikurangi margin (New Zealand): Implications for a mid-Oligocene age of subduction initiation. *Geochemistry, Geophysics, Geosystems*, 23(5), e2021GC010125. https://doi.org/10.1029/2021GC010125
- Vanorio, T., Scotellaro, C., & Mavko, G. (2008). The effect of chemical and physical processes on the acoustic properties of carbonate rocks. *The Leading Edge*, 27(8), 1040–1048. https://doi.org/10.1190/1.2967558
- Villar, M. V., Martín, P. L., & Barcala, J. M. (2005). Modification of physical, mechanical and hydraulic properties of bentonite by thermo-hydraulic gradients. *Engineering Geology*, 81(3), 284–297. https://doi.org/10.1016/j.enggeo.2005.06.012
- Vora, H. B., & Dugan, B. (2019). Porosity-permeability relationships in mudstone from pore-scale fluid flow simulations using the Lattice Boltzmann method. Water Resources Research, 55(8), 7060–7071. https://doi.org/10.1029/2019WR024985
- Wallace, L. M. (2020). Slow slip events in New Zealand. Annual Review of Earth and Planetary Sciences, 48(1), 175–203. https://doi.org/10.1146/annurev-earth-0717190055104
- Wallace, L. M., Saffer, D. M., Barnes, P. M., Pecher, I. A., Petronotis, K. E., & LeVay, L. J. (2019). Hikurangi subduction margin coring, logging, and observatories. In *Proceedings of the international ocean discovery program*. https://doi.org/10.14379/iodp.proc.372B375.102.2019
- Walsh, R. (2011). Compilation and consolidation of field and laboratory data for hydrogeological properties (DGR Site Charact. Doc. No. TR-08-10). Geofirma Eng. Ltd.
- Warren-Smith, E., Fry, B., Wallace, L., Chon, E., Henrys, S., Sheehan, A., et al. (2019). Episodic stress and fluid pressure cycling in subducting oceanic crust during slow slip. *Nature Geoscience*, *12*(6), 475–481. https://doi.org/10.1038/s41561-019-0367-x
- Yohler, R., Bartlow, N., Wallace, L. M., & Williams, C. (2019). Time-dependent behavior of a near-trench slow-slip event at the Hikurangi subduction zone. *Geochemistry, Geophysics, Geosystems*, 20(8), 4292–4304. https://doi.org/10.1029/2019GC008229
- Yu, C., Matray, J.-M., Gonçalvès, J., Jaeggi, D., Gräsle, W., Wieczorek, K., et al. (2017). Comparative study of methods to estimate hydraulic parameters in the hydraulically undisturbed Opalinus Clay (Switzerland). Swiss Journal of Geosciences, 110(1), 85–104. https://doi.org/10.1007/s00015-016-0257-9

References From the Supporting Information

- Arp, V. D., McCarty, R. D., & Friend, D. G. (1998). Thermophysical properties of helium-4 from 0.8 to 1500 K with pressures to 2000 MPa (technical report No. 1334 (revised)). NIST.
- Carmichael, R. S. (Ed.) (1989). Practical handbook of physical properties of rocks and minerals. CRC Press.
- Hill, R. (1952). The elastic behaviour of a crystalline aggregate. Proceedings of the Physical Society Section A, 65(5), 349–354. https://doi.org/10.1088/0370-1298/65/5/307
- Hillier, S. (2000). Accurate quantitative analysis of clay and other minerals in sandstones by XRD: Comparison of a Rietveld and a reference intensity ratio (RIR) method and the importance of sample preparation. *Clay Minerals*, 35(1), 291–302. https://doi.org/10.1180/000985500546666 Hu, B., Zhang, C., & Zhang, X. (2022). The effects of hydrochloric acid pretreatment on different types of clay minerals. *Minerals*, 12(9), 1167. https://doi.org/10.3390/min12091167
- Kerschnitzki, M., Kollmannsberger, P., Burghammer, M., Duda, G. N., Weinkamer, R., Wagermaier, W., & Fratzl, P. (2013). Architecture of the osteocyte network correlates with bone material quality: Osteocyte network architecture correlates with bone material quality. *Journal of Bone and Mineral Research*, 28(8), 1837–1845. https://doi.org/10.1002/jbmr.1927

TISATO ET AL. 10 of 11



Geophysical Research Letters

- 10.1029/2023GL103696
- Komadel, P., Schmidt, D., Madejová, J., & Číčel, B. (1990). Alteration of smectites by treatments with hydrochloric acid and sodium carbonate solutions. *Applied Clay Science*, 5(2), 113–122. https://doi.org/10.1016/0169-1317(90)90017-J
- Kumar, S., Panda, A. K., & Singh, R. K. (2013). Preparation and characterization of acids and alkali treated kaolin clay. *Bulletin of Chemical Reaction Engineering and Catalysis*, 8(1), 61–69. https://doi.org/10.9767/bcrec.8.1.4530.61-69
- Lafuente, B., Downs, R. T., Yang, H., & Stone, N. (2015). 1. The power of databases: The RRUFF project. In T. Armbruster & R. M. Danisi (Eds.), *Highlights in mineralogical crystallography* (pp. 1–30). DE GRUYTER. https://doi.org/10.1515/9783110417104-003
- Lee, T. C., Kashyap, R. L., & Chu, C. N. (1994). Building skeleton models via 3-D medial surface axis thinning algorithms. CVGIP: Graphical Models and Image Processing, 56(6), 462–478. https://doi.org/10.1006/cgip.1994.1042
- Moore, D. M., & Reynolds, R. C. (1997). X-ray diffraction and the identification and analysis of clay minerals (2nd ed.). Oxford University Press. Ortiz-Vega, D., Hall, K., Holste, J., Arp, V., Harvey, A., & Lemmon, E. (2020). Helmholtz equation of state for helium. Journal of Physical and Chemical Reference Data.
- Ostrom, M. E. (1961). Separation of clay minerals from carbonate rocks by using acid. SEPM Journal of Sedimentary Research, 31. https://doi.org/10.1306/74D70B1E-2B21-11D7-8648000102C1865D
- Prelicz, R. M. (2005). Seismic anisotropy in peridotites from the western Gneiss region (Norway): Laboratory measurements at high PT conditions and fabric based model predictions [Application/pdf]. ETH Zurich. https://doi.org/10.3929/ETHZ-A-005115293

TISATO ET AL. 11 of 11